Article

# Liquid-infused nanostructured composite as a high-performance thermal interface material for effective cooling

Rui Cheng ⬤[1,4], Qixian Wang[1,4], Zexiao Wang[1,4], Lin Jing[1,4], Ana V. Garcia-Caraveo ⬤[2], Zhuo Li ⬤[1], Yibai Zhong ⬤[1], Xiu Liu ⬤[1], Xiao Luo ⬤[1], Tianyi Huang[1], Hyeong Seok Yun[1], Hakan Salihoglu[1], Loren Russell[3], Navid Kazem[3], Tianyi Chen ⬤[2] & Sheng Shen ⬤[1] ✉

Effective heat dissipation remains a grand challenge for energy-dense devices and systems. As heterogeneous integration becomes increasingly inevitable in electronics, thermal resistance at interfaces has emerged as a critical bottleneck for thermal management. However, existing thermal interface solutions are constrained by either high thermal resistance or poor reliability. We report a strategy to create printable, high-performance liquid-infused nanostructured composites, comprising a mechanically soft and thermally conductive double-sided Cu nanowire array scaffold infused with a customized thermal-bridge liquid that suppresses contact thermal resistance. The liquid infusion concept is versatile for a broad range of thermal interface applications. Remarkably, the liquid metal infused nanostructured composite exhibits an ultra-low thermal resistance <1 mm² K W⁻¹ at interface, outperforming state-of-the-art thermal interface materials on chip-cooling. The high reliability of the nanostructured composites enables undegraded performance through extreme temperature cycling. We envision liquid-infused nanostructured composites as a universal thermal interface solution for cooling applications in data centers, GPU/CPU systems, solid-state lasers, and LEDs.

Efficient heat dissipation is essential for saving energy and preventing malfunction in all kinds of energy-dense devices and systems[1–4]. Globally, data centers consume about 240–340 terawatt hours of electricity annually (1–1.3% of total electricity used on earth each year), which will continue to grow with the development of cloud computing and artificial intelligence[5,6]. Cooling demands account for as much as 33–40 % of data center energy usage and consume billions of tons of water per year[7]. Meanwhile, heat fluxes of high-power electronics, such as solid-state lasers, wide bandgap transistors, and phased array radars, have reached unprecedented ~1 kW cm⁻² [8], which, without effective thermal solutions, will lead to rapid device performance and

lifetime degradation[9]. As heterogeneous integration becomes increasingly inevitable in future electrical devices and systems[10], thermal resistance at interfaces has emerged as a critical bottleneck for efficient thermal management[11,12]. While thermal interface materials (TIMs), such as solders, greases, compounds, and pads, have been widely applied to alleviate thermal interface resistance[13], they must exhibit both a low bulk thermal resistance and a low contact thermal resistance to ensure optimal thermal performance. In addition, TIM should possess mechanical softness to effectively absorb the thermal stress resulting from the mismatch in coefficient of thermal expansion (CTE) at the interface[14,15]. Meeting these stringent requirements poses

[1]Department of Mechanical Engineering, Carnegie Mellon University, 5000 Forbes Ave, Pittsburgh, PA, USA. [2]College of Engineering, Oregon State University, 1791 SW Campus Way, Corvallis, OR, USA. [3]Arieca, Inc., 201 N Braddock Ave STE 334, Pittsburgh, PA, USA. [4]These authors contributed equally: Rui Cheng, Qixian Wang, Zexiao Wang, Lin Jing. ✉e-mail: sshen1@cmu.edu

formidable challenges in the development of a high-performance multifunctional TIM.

Traditional solders and solderable nanostructured TIMs have high thermal conductivity and low contact resistance but rely on high-temperature soldering processes limited to specific material surfaces, which hinders their applications as universal joints[15–18]. Although polymer composite TIMs such as thermal greases and compounds have high compliance, they struggle with "pump-out" issues, which cause poor reliability, and low thermal performance due to the scattered heat conduction among dispersed conductive fillers[13,14,19]. Compared with liquid-form thermal greases/compounds, solid-state thermal pads are more programmable on the material alignment and thereby can potentially achieve a higher thermal conductivity[20,21]. However, the substantial thickness (typically hundreds-of-μm) caused by the fabrication limitations and direct ("dry") thermal contact with substrates result in high bulk and contact thermal resistances,

compromising their overall thermal performance. To date, there is still a lack of a universal high-performance TIM that can meet the crucial demands of thermal management.

Here, we demonstrate a printable liquid-infused nanostructured composite (LINC) as a universal high-performance TIM. As shown in Fig. 1a, a LINC is comprised of a unique mechanically compliable and thermally conductive double-sided Cu nanowire (CuNW) array scaffold infused with a customized thermal-bridge liquid. Vertically aligned CuNWs with a typical diameter of 200 nm and height of ~25 μm are grown on both sides of a thin Cu foil (~10 μm thick) by scalable templated electrochemical deposition (Fig. 1b–d and Supplementary Fig. S1). Also, the CuNWs have high uniformity with a height difference <3 μm, as shown in Fig. 1b and Supplementary Fig. S2. The double-sided CuNW arrays, alongside the center Cu foil, function as a conductive and compliant scaffold due to the high thermal conductivity of Cu and the high aspect ratio (>100) of
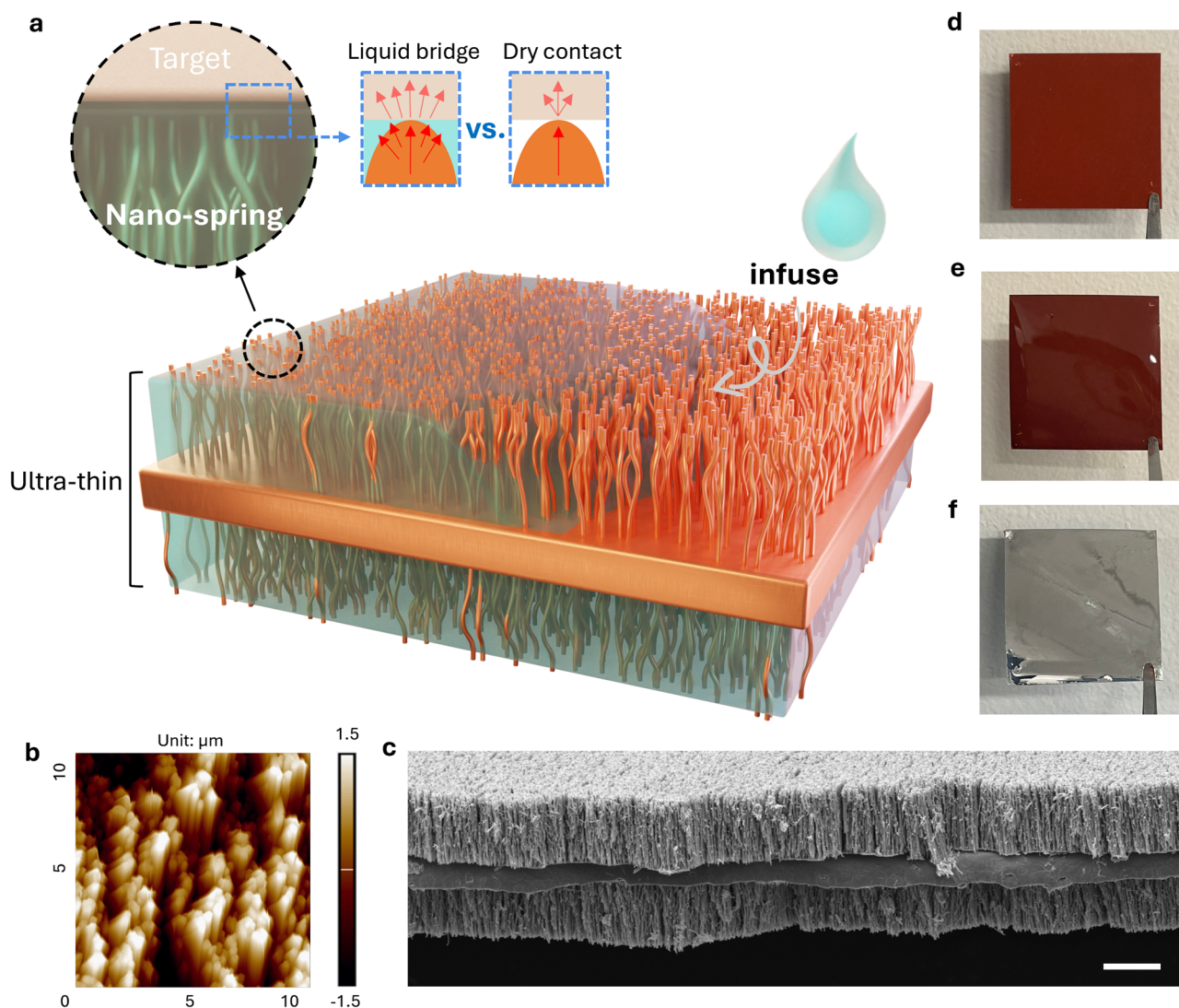


Fig. 1 | **Liquid-infused nanostructured composites (LINCs). a** Schematic illustration of LINCs, where an ultra-thin, mechanically compliant, and thermally conductive double-sided copper nanowire (CuNW) array scaffold is infused with a customized thermal-bridge liquid. CuNW arrays comply with the target surface like "nano-springs" and serve as efficient heat flow channels across the interface. Infused liquid effectively bridges the CuNW tips thermally to the target surface and, therefore, largely suppresses the contact resistance of LINCs. The multifunctional thermal-bridge liquid allows for pre-packaging provides reworkability when using

non-adhesives, and enables thermal bonding of two substrates at room temperature akin to soldering but with extended applicability to non-solderable materials when using adhesives, therefore is highly customizable for a broad range of applications as a universal high-performance thermal interface material (TIM). **b** Top-view atomic force microscopic image of the CuNW scaffold. **c** Cross-sectional scanning electron microscopic (SEM) image of the CuNW scaffold, scale bar, 20 μm. Pictures of (**d**) CuNW scaffold, (**e**) Glycerol-LINC, (**f**) Liquid-Metal-LINC, at the size of ~30 × 30 mm.
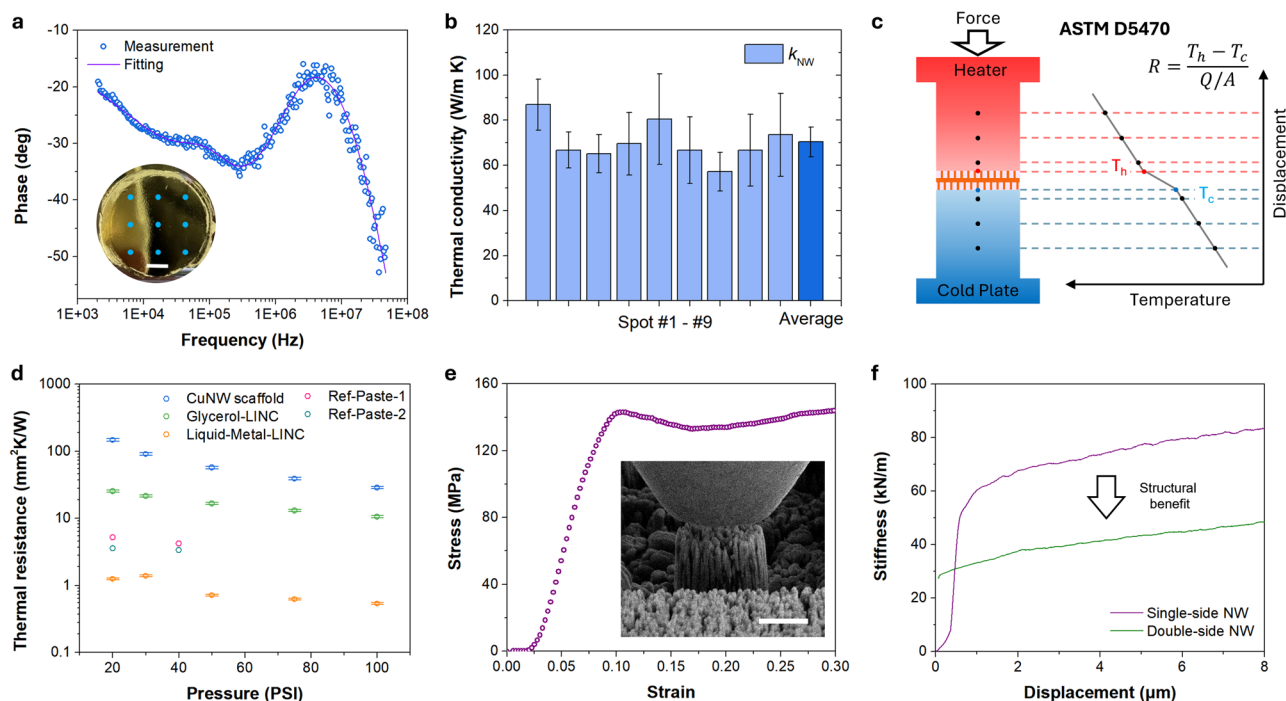
**Fig. 2 | Thermal and mechanical characterization. a** Typical frequency-domain thermal reflectance (FDTR) data plot and the best least-square fitting to the heat transfer model. Inset: picture of tested sample and 9 test spots marked in blue, scale bar, 5 mm. **b** Histograms summarizing thermal conductivity of the copper nanowire (CuNW) array layer extracted from the FDTR measurements at different test spots, error bar data listed in Supplementary Information Table S1. **c** Schematic showing the principle of ASTM D5470 standard thermal measurements. **d** Pressure-dependent thermal resistance of liquid-infused nanostructured composites (LINCs) without and with different thermal-bridge liquids, tested under the ASTM D5470 standard, in which the Liquid-Metal-LINC shows an extremely low thermal resistance (<1 mm$^2$ K W$^{-1}$) above 50 Psi. Two commercially available thermal pastes

with reported thermal conductivities of 8.5 W m K$^{-1}$ and 14.2 W m K$^{-1}$ are measured in the same setup as references, error bar data accessible in Source Data. **e** Stiffness characterization of an isolated CuNW bundle using in situ cylindrical flat punch indentation. Inset: Scanning electron microscopic image of the nanoindentation process on an isolated nanowire bundle, scale bar, 5 μm. **f** Displacement vs Stiffness curve in the continuous stiffness measurement showing the stiffness results for single-sided and double-sided films each from three different indentation locations, where the double-side film shows about half the stiffness measured from the single-sided film, indicating the structural benefit of the double-sided design. Source data are provided as a Source Data file.

CuNWs. The high compliance of CuNW arrays ensures that they conform to the morphology of an object surface like "nano-springs", thereby serving as efficient heat flow channels across the interface. By transforming the nanowire-surface point-to-point "dry" contact into nanowire/liquid-surface composite contact, our novel liquid infusion method can effectively bridge the CuNW tips thermally to a target surface and therefore largely suppress the contact resistance of LINCs, considering that the thermal conductivity of liquids is usually more than one order of magnitude larger than that of air. When employing a high thermal conductivity infused liquid, such as liquid metal, it also contributes to the substantial reduction of the bulk thermal resistance of LINCs. Hence, in contrast with existing TIM studies that primarily focus on reducing the bulk resistance, LINCs simultaneously achieve a low bulk resistance and a low contact resistance, both of which are equally crucial aspects in practical applications. Moreover, the infused liquid is multifunctional and highly customizable for a broad range of applications. As shown in Fig. 1e, f, when using non-adhesive liquids (e.g., non-volatile solvents, liquid metals, etc.), LINCs allow for pre-packaging and provide high reworkability, facilitating convenient and repeated uses (Supplementary Movie S1). Unlike the high-temperature soldering process with restricted material compatibility, the utilization of a low-viscosity liquid adhesive (e.g., resin, super glue, etc.) in LINCs enables thermal bonding of two substrates at room-temperature (Supplementary Fig. S3a, b), which not only maintains strong structural integrity at the interfaces akin to soldering but also expands its applicability to non-solderable materials such as polymers and ceramics.

## Results and discussion
### Thermal and mechanical characterization of LINCs
We implement the well-established frequency-domain thermoreflectance (FDTR) method[22–24] to measure the bulk thermal properties of the CuNW scaffold in LINCs (Supplementary Text S1). The FDTR method is a pump-probe optical technique in which the modulated pump beam excites the sample while the probe beam measures the changes in the temperature-dependent reflectance. The phase lag between the pump and probe lasers is measured as a function of the modulation frequency, where the thermal properties including in-plane and cross-plane thermal conductivities and thermal interface resistance of the sample can be extracted by fitting the measured data to a 2D heat conduction model for multilayer thin films (Supplementary Fig. S4)[22,24]. A typical data plot is presented in Fig. 2a with a photo of the tested sample included as inset. Figure 2b summarizes thermal conductivity measurements of the CuNW layer fitted from the phase-frequency plots obtained from 9 different locations on the sample. The average thermal conductivity of the CuNW layer is determined to be 70.4 ± 13.9 W m$^{-1}$ K$^{-1}$, corresponding to a thermal resistance of 0.36 ± 0.07 mm$^2$ K W$^{-1}$ (Supplementary Text S2 and Table S1). The measured thermal conductivity of the 10 μm Cu foil in the middle of LINCs is 376.6 ± 37.7 W m$^{-1}$ K$^{-1}$ with an effective bulk resistance of 0.027 ± 0.003 mm$^2$ K W$^{-1}$. The thermal contact resistances at CuNW/Cu-base interfaces are determined to be 0.027 ± 0.005 mm$^2$ K W$^{-1}$. The overall effective thermal conductivity of the CuNW scaffold is 76.0 ± 13.6 W m$^{-1}$ K$^{-1}$, corresponding to the thermal resistance of 0.79 ± 0.14 mm$^2$ K W$^{-1}$. Therefore, CuNW layers give rise to the majority (91.1%) of the total thermal resistance of the CuNW scaffold. In addition
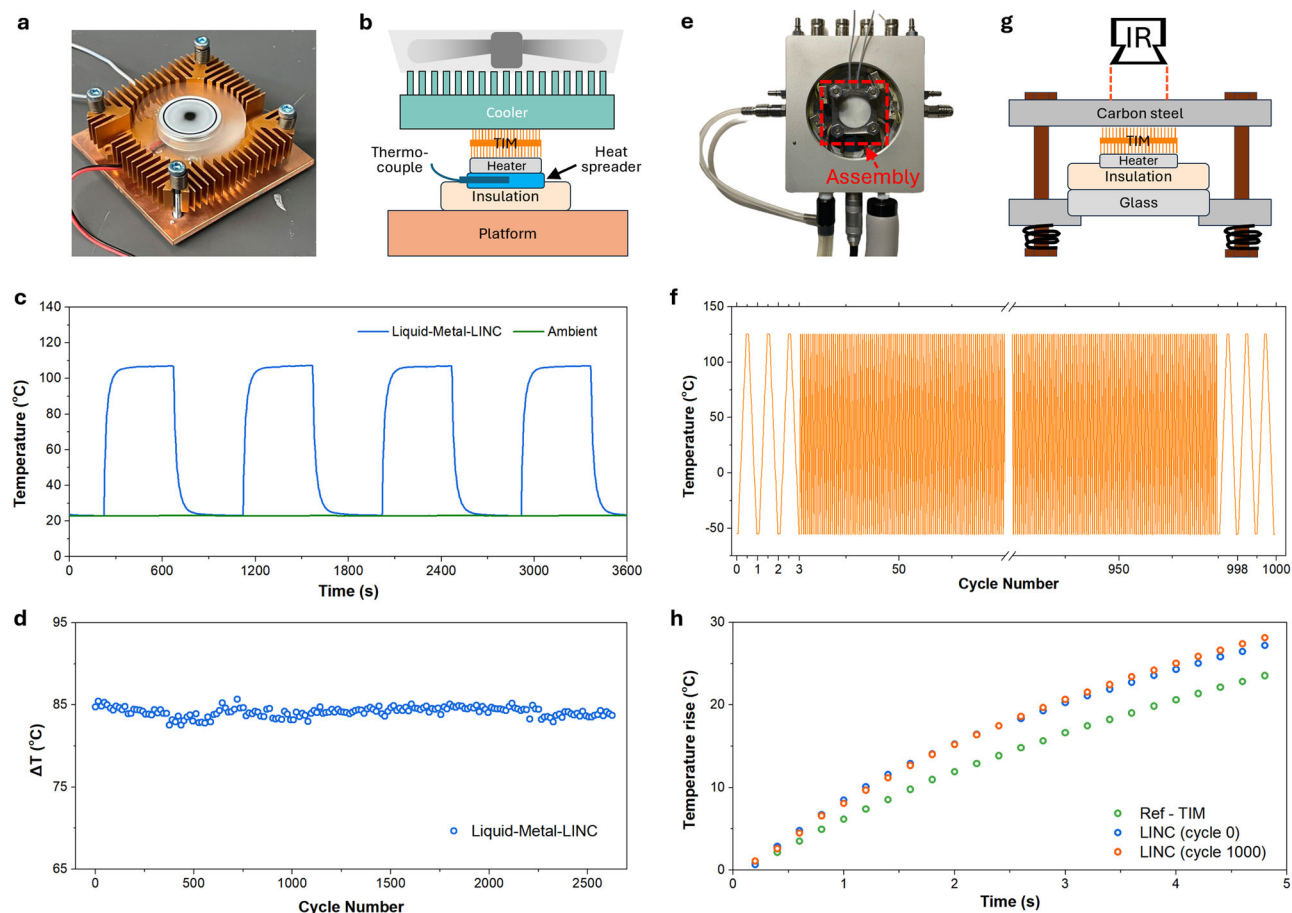
**Fig. 3 | In situ power cycling and temperature cycling tests of liquid-infused nanostructured composites (LINCs). a** Real image, and (**b**) a schematic of the in situ power cycling test setup for testing the cycling stability of thermal interface materials (TIMs). **c** Typical cycling temperature profile of Liquid-Metal-LINC. **d** Measured temperature difference between the ambient and equilibrium heater temperature for >2600 power cycles. The Liquid-Metal-LINC shows high reliability with no obvious performance degradation. **e** Picture of the assembly mounted on a Linkam stage equipped with a liquid nitrogen pump to control the temperature precisely and rapidly. **f** 1000-cycle accelerated aging test under an extreme temperature range from − 55 °C to 125 °C using the Linkam stage. **g** Schematic showing the temperature history measurement before and after temperature cycles, where a thermal infrared microscope is used to monitor the top surface temperature of the carbon-steel substrate when the built-in 38 W ceramic heater is turned on. **h** Real-time carbon-steel substrate surface temperature data. The Liquid-Metal-LINC assembly shows stable thermal performance after 1000 cycles. Source data are provided as a Source Data file.

to vertical heat conduction, the CuNW scaffold also has a large lateral thermal conductivity of $69.5 \pm 16.1 \, W \, m^{-1} K^{-1}$ because of the highly conductive Cu-base layer in the middle and the laterally cross-linked CuNWs on both sides (Supplementary Text S3). The Cu-base layer further performs as a lateral heat spreader to increase heat flux uniformity and mitigate the local hot spot issue. Therefore, LINCs can synergistically regulate heat flow along an interface in both vertical and lateral directions, offering an advantage over vertically aligned nanowires[16–18], graphene[20,21,25], CNTs[26,27], polymer fibers[28], and semiconductor pillars[29,30] that mainly regulate heat conduction in the vertical direction.

Following the ASTM D5470 standard, the overall thermal resistance of LINCs, including both bulk and contact resistances, is characterized through the 1D thermal measurement, as depicted in Fig. 2c. A pressure-dependent thermal performance of LINCs with different infused liquids is obtained through progressively increasing the mechanical load from approximately 20 to 100 Psi. As illustrated in Fig. 2d, the overall thermal resistances of the bare CuNW scaffold, Glycerol-LINC, and Liquid-Metal-LINC consistently decrease with increased pressure. Under 100 Psi, the bare CuNW scaffold shows a large overall thermal resistance of $28.72 \pm 1.14 \, mm^2 \, K \, W^{-1}$, which is notably suppressed to $10.53 \pm 0.36 \, mm^2 \, K \, W^{-1}$ with glycerol infusion,

and remarkably, $<1.0 \, mm^2 \, K \, W^{-1}$ with liquid metal infusion. Two commercially available thermal pastes with reported thermal conductivity of $8.5 \, W \, m^{-1} K^{-1}$ and $14.2 \, W \, m^{-1} K^{-1}$ are measured in the same setup as references, showing thermal resistance of $3 \sim 6 \, mm^2 \, K \, W^{-1}$. Our Liquid-Metal-LINC achieves an ultra-low thermal resistance $<1.0 \, mm^2 \, K \, W^{-1}$ under the ASTM D5470 standard at the pressure of 50 Psi, surpassing the previously reported TIMs.

We also measure the mechanical characteristics of CuNW arrays via in situ cylindrical flat punch (diameter ~10 μm) indentation monitored under SEM (Fig. 2e, Supplementary Text S4, and Movie S2). Since the CuNW array in this work is partially cross-linked (Fig. 1c), we use focus ion beam milling to obtain an isolated CuNW bundle with a diameter of ~10 μm so that the influence from the cross-linked CuNW structure on the indentation experiment can be eliminated. With in situ monitoring under SEM, the cylindrical flat punch is located right on top of the isolated CuNW bundle. As a result, the array of CuNWs with an aspect ratio of ~125 exhibits a low Young's modulus of ~2.5 GPa, which is about two orders of magnitude lower than that of bulk Cu. Furthermore, the stiffness of the double-sided CuNW array film is found to be only half that of the monolayer CuNW array structure (Fig. 2f), which can thereby better accommodate the object morphology.
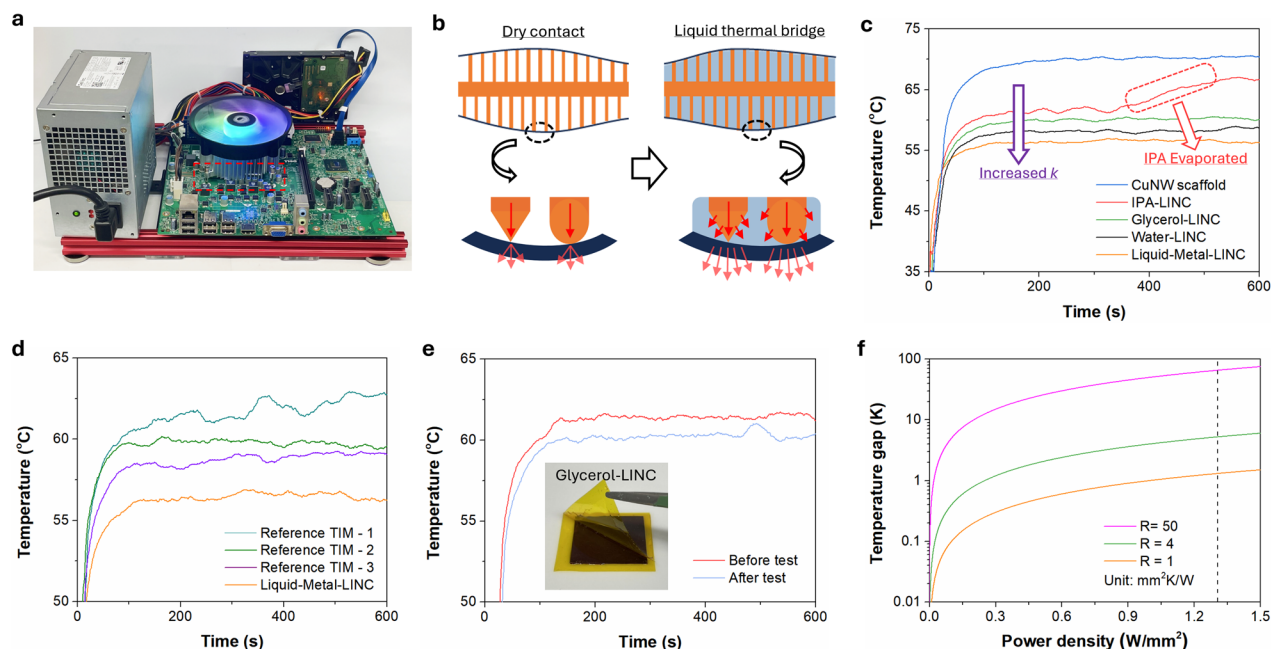
**Fig. 4 | Demonstration of CPU cooling tests. a** Home-built open desktop test station equipped with a 65 W standard office level CPU and an air cooler, right-side pictures showing the thermal grease and LINCs applied on the tested CPU. **b** Schematics showing the mechanism of the thermal bridging effect from the infused liquid, where the nanowire-surface point-to-point "dry" contact is transformed into the nanowire/liquid-surface composite contact with largely suppressed contact resistance. **c** Temperature data of the tested CPU at full load when using liquid-infused nanostructured composites (LINCs) without and with different thermal-bridge liquids. Thermal conductivity ($k$) of air, IPA, glycerol, water, and liquid metal is around 0.024, 0.140, 0.287, 0.600, and 73 W m K$^{-1}$, respectively. The improved heat dissipation with increased $k$ and the observed two-stage temperature behavior of the IPA bridged interface clearly verify the thermal transport mechanism by thermal-bridge liquids. **d** Temperature data of the tested CPU at full load when benchmarking state-of-the-art thermal interface materials (TIMs) with the Liquid-Metal-LINC. Reference TIMs 1, 2, and 3 are widely used thermal greases and phase change material pads with claimed thermal conductivities of 3.8, 8.5, and 14.2 W m K$^{-1}$, respectively. **e** Temperature data of the tested CPU at full load using the Glycerol-LINC before and after 20-time assembling and disassembling. The stable thermal performance indicates the robust reworkability of LINCs. **f** Thermal model simulating the interfacial temperature gap reduction at different power densities, where a ~ 4 K temperature reduction would occur when the TIM thermal resistance is decreased from 4 mm$^2$ K W$^{-1}$ to 1 mm$^2$ K W$^{-1}$. Source data are provided as a Source Data file.

## In situ power cycling and extreme temperature cycling of LINCs

Both power and temperature cycling experiments are conducted to evaluate the long-term reliability of LINCs. We establish an in situ power cycling setup (Fig. 3a, b) equipped with a ceramic heater and an active air-cooler. In our power cycling tests, the CTE mismatch between the metal heat sink and the ceramic heater is ~ 4 times. With a constant cooling power, the heater is periodically turned on and off to cycle the TIMs from room temperature to an equilibrium temperature of >100 °C (Fig. 3c). A high heating power density of ~ 46 W/cm$^2$ is applied to magnify the temperature difference between the ambient and equilibrium (maximum) heater temperature, $\Delta T = T_{heater} - T_{ambient}$, which directly indicates the thermal performance of the TIMs. The degradation of the TIM performance can be observed in real-time through monitoring $\Delta T$. As shown in Fig. 3d for >2600 cycles, our Liquid-Metal-LINC shows no observable degradation during the entire test period. The high reliability of our Liquid-Metal-LINC may be attributed to its composition as a metal composite, which eliminates "dry-out" issues. In addition, the hydrophilicity and friction with CuNWs can effectively trap the infused liquid, preventing it from being pumped out. As shown in Supplementary Fig. S5, pure liquid metal tends to form droplets and leak from the interface, while our Liquid-Metal-LINC retains the minor squeezed liquid metal and mitigates its movement.

We carry out a 1000-cycle temperature cycling test on our Liquid-Metal-LINC under an extreme temperature range from − 55 °C to 125 °C, which is an industrial standard test condition. As shown in Fig. 3e and Supplementary Fig. S6, we first apply the Liquid-Metal-LINC between a carbon-steel substrate and a ceramic heater, which gives rise to a ~ 4-time CTE mismatch. The whole

assembly is then integrated onto a Linkam stage equipped with a liquid nitrogen pump for precise and rapid temperature control, with the carbon-steel surface in thermal contact with the stage. For each cycle, it takes 2 min to rise from − 55 °C to 125 °C and 30 s for dwelling, then 2 min for ramping down to − 55 °C and maintaining the temperature for another 30 s (Fig. 3f). To characterize the thermal performances of the Liquid-Metal-LINC before and after temperature cycling, we employ a thermal infrared microscope to monitor the temperature history of the carbon-steel surface when turning on the built-in ceramic heater to provide ~ 38 W heating power to the assembly, shown in Fig. 3g. Under the same heating condition, Fig. 3h shows the real-time temperature data of the hot spot before and after the temperature cycling test. The temperature rises of the Liquid-Metal-LINC sample before (0 cycle) and after 1000 cycles almost overlap with each other, which indicates consistent thermal transport behavior and, thus, high reliability. As a reference experiment, we also measure the temperature rise of a commercial high-performance graphite thermal pad based on the same assembly, which exhibits a more sluggish temperature rise due to the larger thermal resistance.

Considering that the viscosity of the infused liquid may change with temperature and impact the LINC performance, we further conducted a high-power constant heating experiment on the Epoxy-Resin-LINC (Supplementary Figs. S7a, b). We specifically choose an epoxy resin with low initial viscosity and negligible shrinkage after setting. A hydraulic cooler is used to maintain a low working temperature, thus enabling slow curing of the epoxy resin. Throughout the curing process, its viscosity changes from 300 cP to infinity (fully cured solid). In Supplementary Fig. S7c, there is no observable temperature change

during the curing process, indicating a negligible impact of viscosity change on the thermal performance.

Mechanical reliability of LINCs under repeated thermal stress is further studied via a repeated compression test on a Glycerol-LINC with results presented in Supplementary Figs. S8, S9, and Text S5. A rebound effect on thermal performance in the LINC sample is observed when pressure is released, clearly demonstrating the "nano-spring" effect. However, gradual degradation of this "nano-spring" behavior is observed with repeated compression, suggesting that some nanowires may undergo plastic deformation, permanently conforming to the surface roughness of the object under high pressure (e.g., 80 psi).

### Demonstration of CPU cooling and liquid thermal bridge

We directly apply the LINC on a CPU ($\sim 29 \times 29$ mm$^2$) for heat dissipation tests (Fig. 4). A home-built open desktop equipped with a 65 W standard office-level CPU and an air cooler is assembled as the test platform with consistent heat flow and mounting pressure (Fig. 4a). We evaluate the cooling performance of LINCs by monitoring the temperature of the CPU at full load (monitored to be consistently ~69 W) using its built-in temperature sensors under similar ambient temperature (<1 °C fluctuation) and cooling conditions. Here, LINCs are tested under the CPU platform with different infused liquids to elucidate the thermal transport mechanism and the function of thermal-bridge liquids. When using the CuNW scaffold solely as a TIM, the contacts between the nanowire tips and the target surface are limited to point-to-point "dry" thermal contacts (Fig. 4b), which results in a high CPU temperature of ~70 °C due to the large thermal contact resistance (Fig. 4c). When glycerol is applied as the thermal-bridge liquid on the same CuNW scaffold (Fig. 4c), the CPU temperature is significantly decreased to ~60 °C. Since the thermal conductivity of glycerol (~0.3 W m$^{-1}$ K$^{-1}$) is two orders of magnitude lower than the CuNW scaffold and barely contributes to the bulk thermal conductivity of the composite layer, the substantial improvement in thermal performance is mainly attributed to the infused liquid that thermally bridges the nanowire tips and the target surface with a low contact resistance (Fig. 4b). When using adhesives such as epoxy resin and polydimethylsiloxane (PDMS) for permanent bonding, the resulting full-load CPU temperature is also ~60 °C (Supplementary Fig. S3c). To verify the contribution of the thermal-bridge liquids, evaporative isopropanol alcohol (IPA) is applied with the same CuNW scaffold. We observe that the full-load CPU temperature first stabilizes at ~62 °C, for ~4 min but then rises to over 67 °C indicating the loss of bridging effects after the evaporation of IPA. In Fig. 4c, it is evident that a liquid with higher thermal conductivity, such as water (~0.6 W m$^{-1}$ K$^{-1}$), enhances the overall performance of LINCs (~58 °C) as compared to a liquid with lower thermal conductivity, like glycerol or IPA, by further reducing the contact resistance. To maximize the thermal performance of LINCs, the LINC infused with a liquid metal further decreases the CPU temperature to ~56 °C in our test platform. We benchmark the Liquid-Metal-LINC with commercially available state-of-the-art TIMs in Fig. 4d. Compared with Reference TIM 2 (high-performance phase-change material, reported thermal conductivity: ~8.5 W m$^{-1}$ K$^{-1}$) and Reference TIM 3 (high-performance thermal grease, reported thermal conductivity: ~14.2 W m$^{-1}$ K$^{-1}$), our Liquid-Metal-LINC demonstrates superior thermal performance by further reducing the CPU temperature for >2 °C, which corresponds to a chip-to-coolant efficiency improvement for >5%. With the non-volatile solvents (e.g., glycerol, oil), LINCs can be pre-packaged for easy applications and achieve high reworkability. As shown in Fig. 4e and Supplementary Movie S1, the CPU test platform using the Glycerol-LINC is disassembled and assembled more than 20 times to simulate the reconfiguring process. Consistently, steady-state CPU temperatures of ~60 °C are observed before and after the process, indicating the stable performance of LINCs with robust reworkability. In Fig. 4f, we estimate the contribution of the TIM performance evolution using a thermal model (Supplementary Text S6). For modern high-end chips with high thermal design power density (e.g., NVIDIA AD102, ~1.3 W mm$^{-2}$), the thermal interface resistance reduction from 4 mm$^2$ K W$^{-1}$ to 1 mm$^2$ K W$^{-1}$ can contribute to up to 4 K reduction on the interfacial temperature gap and benefit the chip cooling, especially for data centers where the chip-to-coolant temperature difference is typically smaller than 30 K.

In summary, we report a printable LINC as a versatile and high-performance TIM. In the LINC scheme, the high thermal conductivity (>76 W m$^{-1}$ K$^{-1}$) of the CuNW scaffold achieves a low bulk thermal resistance, whereas the infusion of thermal-bridge liquids effectively mitigates the contact resistance and results in a significant reduction of overall resistance from $28.72 \pm 1.14$ mm$^2$ K W$^{-1}$ for the bare CuNW scaffold to an ultra-low value of <1.0 mm$^2$ K W$^{-1}$ for the Liquid-Metal-LINC under ASTM D5470 standard tests. With a compliant and hydrophilic CuNW array on both sides serving as a "nano-spring" and retaining the infused liquid, LINCs demonstrate stable performance in both >2600 power cycles and 1000 temperature cycles over wide temperature ranges and large CTE mismatch. In the CPU cooling test, our Liquid-Metal-LINC demonstrates overperformed thermal performance as compared to state-of-the-art TIMs. The highly customizable nature of thermal-bridge liquids allows LINCs to be either mechanically bonded like soldering or highly reworkable as a thermal pad. Overall, LINCs facilitate a substantial reduction in interfacial thermal resistance while maintaining robust reliability. LINCs thus show high potential for enhancing the thermal management of energy-dense devices and systems, contributing to future energy efficiency and sustainability.

## Methods
### Fabrication of LINCs
High-purity (99.9%) Cu foil with a thickness of ~10 or ~20 μm is used as the "Cu base" and sandwiched between two hydrophilic track-etched polycarbonate (TEPC) template films with pore-size of 200 nm or 800 nm and thickness of ~25 or ~50 μm (Millipore). The Cu electroplating is then conducted on the Cu foil in a Cu electrolyte bath (Sigma-Aldrich) to allow the direct growth of CuNW arrays inside the TEPC template films (Supplementary Fig. S1). After that, the sample is washed sequentially with deionized water and IPA and dried gently by a nitrogen gun. Templated films are then etched/dissolved via dichloromethane bath immersion. Thermal bridge liquids are then drop casted on top of the resulting hydrophilic CuNW array and infused into the nanostructure driven by capillary force. The oxide shell and high surface tension of liquid metal require one more step of acid treatment. All the liquids that are infused in LINCs are based on the hydrophilicity between the liquids and the nanostructured Cu scaffold. When using an adhesive as the thermal-bridge liquid, the obtained CuNW scaffold is rinsed with adhesive liquid or precursors (e.g., glue, resin, epoxy, etc.) and inserted in the target interface. Under mild pressure, the soft CuNW arrays conform to the mating surface morphology and direct contact with the surface, while the glue precursors cure with time/heat and maintain the interface integrity. When using a non-adhesive liquid as the thermal-bridge liquid, the scaffold film can either be pre-packaged in protection layers with the pre-infiltrated liquid or simply rinsed with the liquid before being applied in the target interface.

### ASTM D5470 standard thermal characterization
In compliance with the ASTM D5470 protocol, the TIMA 5 system (Nanotest), a 1D steady-state measurement apparatus, is employed for evaluating the thermal properties of LINC samples. The experimental steps involve positioning the sample between two Cu bars, subjecting it to a gradually increasing load ranging from 10 to 100 Psi. Heat flow through the bars is quantified using three thermocouples on each bar, with calculations grounded in Fourier's law. The interface temperature

of the sample is extrapolated based on the location and readings of the six resistance temperature detectors (RTDs) with an uncertainty of 0.2 K and an interfacial temperature uncertainty of 0.05 K. The effective thermal resistance is calculated by dividing the temperature differential across the sample by the average heat flux between the two Cu bars, following the equation: $R = \frac{T_h - T_c}{Q/A}$. Noteworthily, the extremely low thermal resistance of the Liquid-Metal-LINC is below the measurement limit of the test platform of $1\,mm^2\,K\,W^{-1}$, so we report the value as being lower than $1\,mm^2\,K\,W^{-1}$ instead of the exact recorded value.

### Mechanical characterization
Cylindrical flat punch indentation is performed on the single-sided and double-sided CuNW array films. The flat punch indenter has a nominal diameter of $10\,\mu m$. Indentation is performed under the displacement control mode with a displacement rate of $0.1\,\mu m\,s^{-1}$. The continuous stiffness measurement (CSM) method is applied to measure the stiffness, which indicates the relative softness of the material under compression. The CSM is set as a displacement control mode with a frequency of 100 Hz and an amplitude of $0.003\,\mu m$. Focused ion beam milling is performed to isolate a CuNW bundle with a diameter of approximately $10\,\mu m$ to eliminate the influence of the surrounding cross-linked CuNW structure on the tested area, which matches the size of the flat punch tip. An in situ indentation monitored under SEM is essential for accurately positioning the flat punch tip directly on top of the isolated CuNW bundle. For a double-sided CuNW array film, flat-punch indentation is directly performed on 3 random locations.

### Power cycling and in situ degradation monitoring
In the tests, the Liquid-Metal-LINC is assembled between a copper-coated aluminum air-cooler and a ceramic heater (28 V, ~ 1.65 A, ~ 46 W, $1 \times 1\,cm^2$) with a clamping pressure controlled by standard screws and springs (Fig. 3a, b). A size-matched copper heat spreader with an inserted k-type thermocouple is attached to the back side of the ceramic heater. The bottom side of the heat spreader is thermally insulated by a silicone sheet. For each power cycle, the heater is turned on for 450 s and off for 450 s, with the cooler running at full load. Thermocouple data are collected through an Omega data collection hub at 0.36 Hz. The last 15 data points of each cycle are averaged to represent the equilibrium temperature of each cycle. The equilibrium temperature data for every 15 cycles are shown in Fig. 3d.

### Temperature cycling and degradation analysis
The TIM is applied between a 2 mm thick carbon-steel sheet and a ceramic heater (24 V, ~ 1.6 A, ~ 38 W, $1.5 \times 1.5\,cm^2$) with a mild pressure (<40 Psi) controlled by standard screws and springs (Fig. 3g and Supplementary Fig. S6). The back side of the heater is thermally insulated by a silicone sheet on top of a glass plate. The assembly is mounted onto the Linkam stage (HFS600E) equipped with a liquid nitrogen pump (LNP96) to control the temperature precisely and rapidly (Fig. 3e). A thin layer of thermal grease is applied between the assembly and the Linkam stage surface to reduce the thermal barrier. The cycle profile applied to the stage is as follows: 2 min from $-55\,°C$ to $125\,°C$ and dwelling for 30 s, then 2 min ramping down to $-55\,°C$ and keeping the temperature for another 30 s. To characterize the thermal performance before and after thermal cycling, we employ a thermal infrared microscope (QFI InfraScopeTM) to measure the temperature history of the carbon-steel top surface immediately after turning on the 38 W built-in ceramic heater (Supplementary Fig. S6). With a silicone sheet insulating the back side of the ceramic heater, heat is mainly conducted to the carbon-steel substrate. In this case, any change in the TIM performance can be observed from the temperature response curve. A reference graphite thermal pad is also subjected to the same procedure. The infrared imaging data are processed by averaging the hot-spot region of the same size and plotted in Fig. 3h.

### CPU cooling demonstration
A home-built open desktop equipped with a 65 W standard office-level CPU (Intel Xeon E3-1225 3.1 GHz, actual operating power ~ 69 W) and an air cooler is assembled as the test platform. Both the CPU and radiator surfaces are lightly polished before testing to ensure a non-bent, original state to rule out possible interferences. The open-source software FurMark is used to concurrently stress the CPU & integrated GPU at 100% workload, while another open-source software, Open-HardwareMonitor is used to record the real-time core temperature, power consumption, and core frequency of the CPU from the built-in sensors. All the tests are conducted at a monitored room temperature of around $22\,°C$. All the TIMs are properly applied following instructions and fairly compared under the same setup and pressure.

## Data availability
The authors declare that the main data supporting the findings of this study are contained within the paper and its associated Supplementary Information. All other relevant data are available from the corresponding author upon reasonable request. Source data are provided in this paper.

## References
1. van Erp, R. et al. Co-designing electronics with microfluidics for more sustainable cooling. *Nature* **585**, 211–216 (2020).
2. Gebrael, T. et al. High-efficiency cooling via the monolithic integration of copper on electronic devices. *Nat. Electron.* **5**, 394–402 (2022).
3. Li, Y. et al. Transforming heat transfer with thermal metamaterials and devices. *Nat. Rev. Mater.* **6**, 488–507 (2021).
4. Mao, J., Chen, G. & Ren, Z. Thermoelectric cooling materials. *Nat. Mater.* **20**, 454–461 (2021).
5. Mytton, D. & Ashtine, M. Sources of data center energy estimates: A comprehensive review. *Joule* **6**, 2032–2056 (2022).
6. Masanet, E. et al. Recalibrating global data center energy-use estimates. *Science* **367**, 984–986 (2020).
7. Shehabi, A. et al. *United States Data Center Energy Usage Report* (2016).
8. Bar-Cohen, A., Maurer, J. J. & Sivananthan, A. Near-junction microfluidic cooling for wide bandgap devices. *MRS Adv.* **1**, 181–195 (2016).
9. Bansode, P. V. et al. Measurement of the thermal performance of a custom-build single-phase immersion cooled server at various high and low temperatures for prolonged time. *J. Electron. Packag.* **142**, 011010 (2020).
10. Fischer, A. C. et al. Integrating MEMS and ICs. *Microsyst. Nanoeng.* **1**, 1–16 (2015).
11. McNamara, A. J., Joshi, Y. & Zhang, Z. Characterization of nanostructured thermal interface materials–a review. *Int. J. Therm. Sci.* **62**, 2–11 (2012).
12. Prasher, R. Thermal interface materials: historical perspective, status, and future directions. *Proc. IEEE* **94**, 1571–1586 (2006).
13. Hansson, J. et al. Novel nanostructured thermal interface materials: a review. *Int. Mater. Rev.* **63**, 22–45 (2018).
14. Razeeb, K. M. et al. Present and future thermal interface materials for electronic devices. *Int. Mater. Rev.* **63**, 1–21 (2018).
15. Bar-Cohen, A., Matin, K. & Narumanchi, S. Nanothermal interface materials: technology review and recent results. *J. Electron. Packag.* **137**, 040803 (2015).
16. Barako, M. T. et al. Dense vertically aligned copper nanowire composites as high performance thermal interface materials. *ACS Appl. Mater. Interfaces.* **9**, 42067–42074 (2017).

17. Gong, W. et al. Ultracompliant heterogeneous copper–tin nanowire arrays making a supersolder. *Nano Lett.* **18**, 3586–3592 (2018).
18. Jing, L. et al. 3D Graphene-nanowire "Sandwich" thermal interface with ultralow resistance and stiffness. *ACS Nano.* **17**, 2602–2610 (2023).
19. Bartlett, M. D. et al. High thermal conductivity in soft elastomers with elongated liquid metal inclusions. *Appl. Phys. Sci.* **114**, 2143–2148 (2017).
20. Zhang, Y.-F. et al. High-performance thermal interface materials consisting of vertically aligned graphene film and polymer. *Carbon* **109**, 552–557 (2016).
21. Dai, W. et al. A paper-like inorganic thermal interface material composed of hierarchically structured graphene/silicon carbide nanorods. *ACS Nano.* **13**, 1547–1554 (2019).
22. Schmidt, A. J., Cheaito, R. & Chiesa, M. A frequency-domain thermoreflectance method for the characterization of thermal properties. *Rev. Sci. Instrum.* **80**, 094901 (2009).
23. Regner, K. T. et al. Broadband phonon mean free path contributions to thermal conductivity measured using frequency domain thermoreflectance. *Nat. Commun.* **4**, 1640 (2013).
24. Jing, L. et al. High thermal conductivity of sandwich-structured flexible thermal interface materials. *Small* **19**, 2207015 (2023).
25. Dai, W. et al. Metal-level thermally conductive yet soft graphene thermal interface materials. *ACS Nano.* **13**, 11561–11571 (2019).
26. Balandin, A. A. Thermal properties of graphene and nanostructured carbon materials. *Nat. Mater.* **10**, 569–581 (2011).
27. Cola, B. A. et al. Photoacoustic characterization of carbon nanotube array thermal interfaces. *J. Appl. Phys.* **101**, 054313 (2007).
28. Singh, V. et al. High thermal conductivity of chain-oriented amorphous polythiophene. *Nat. Nanotechnol.* **9**, 384–390 (2014).
29. Cui, Y. et al. Flexible thermal interface based on self-assembled boron arsenide for high-performance thermal management. *Nat. Commun.* **12**, 1284 (2021).
30. Liang, Z. et al. General, vertical, three-dimensional printing of two-dimensional materials with multiscale alignment. *ACS Nano.* **13**, 12653–12661 (2019).

## Author contributions
R.C. and S.S. conceived the idea and designed the experiments. R.C., Q.W., Z.W., and L.J. prepared the samples. R.C., Q.W., Z.W., L.J., and T.H. conducted material and thermal characterizations. L.R. and N.K. contributed to the ASTM D5470 standard thermal characterization. R.C., Q.W., Z.W., Z.L., and Y.Z. built the demonstration on a real computer. Q.W., A.G.C., and T.C. did the mechanical characterization. R.C., Q.W., Z.W., L.J., and X.L. contributed to the thermal mapping and stability test. X.L., H.Y., and H.S. contributed to the additional discussion on overall ideas. S.S., R.C., L.J., Q.W., and Z.W. wrote the manuscript. S.S. supervised this research.

## Competing interests
Pending patent applications No. PCT/US23/21452, PCT/US23/21477, PCT/US24/52805 (S.S. and R.C.), PCT/US24/49718 (S.S., R.C., Q.W., and Z.W.). The remaining authors declare no competing interests.

## Additional information
**Supplementary information** The online version contains supplementary material available at https://doi.org/10.1038/s41467-025-56163-8.

**Correspondence** and requests for materials should be addressed to Sheng Shen.

**Peer review information** *Nature Communications* thanks the anonymous reviewer(s) for their contribution to the peer review of this work. A peer review file is available.

**Reprints and permissions information** is available at http://www.nature.com/reprints

**Publisher's note** Springer Nature remains neutral with regard to jurisdictional claims in published maps and institutional affiliations.